Photon Statistics as a Tool to (Dis)Prove Cooperative Energy Transfer Quantum Cutting in Near-Infrared Emitting Materials

Vincent R.M. Benning[†,‡], Nils van de Mortel[†], Midas Waakop Reijers[†], Maurits Mastwijk[‡], Sander J.W. Vonk[§], Andries Meijerink[‡], Freddy T. Rabouw[†,‡,*]

[†] Soft Condensed Matter and Biophysics, Debye Institute for Nanomaterials Science, Utrecht University, Princetonplein 1, 3584 CC Utrecht, the Netherlands

[‡] Condensed Matter and Interfaces, Debye Institute for Nanomaterials Science, Utrecht University, Princetonplein 1, 3584 CC Utrecht, the Netherlands

[§] Optical Materials Engineering Laboratory, Department of Mechanical and Process Engineering, ETH Zurich, Leonhardstrasse 21, 8092 Zurich, Switzerland

[*] Corresponding author: f.t.rabouw@uu.nl

S1 Sample fabrication & characterization

Y_2O_3 (Merck, 99.99%), Yb_2O_3 (Smart Elements, 99.99%), Tb_4O_7 (Rhône-Poulenc, 99.99%), $(NH_4)_2HPO_4$ (Merck, $\geq 98\%$), CeO_2 (Merck, unspecified purity) and α-Al_2O_3 (Alfa Aesar, 99.9%) were used for the synthesis without any further purification. The phosphors were prepared using a solid-state reaction. For the YPO_4:2% Tb^{3+}, 15% Yb^{3+} sample stoichiometric amounts of precursor were combined with a 10 mol-% excess of $(NH_4)_2HPO_4$ and crushed using a mortar and pestle. The mixture was transferred to an alumina crucible and placed in a tube oven. Next, the furnace was flushed with forming gas (90 vol-% N_2, 10 vol-% H_2) for 1 hour, followed by heating to 1350 °C with a heating rate of 600 °C/hour. The sample was annealed for 2 hours at the set temperature. The YAG:0.1% Ce^{3+}, 5% Yb^{3+} sample was prepared by mixing stoichiometric amounts of precursor with an 20 mol-% excess of α-Al_2O_3. The furnace was flushed with N_2 gas for 3 hours, followed by heating to 1750 °C with a heating rate of 200 °C/hour. The sample was then annealed for 4 hours. Both calcined powders were left to cool to room temperature and were subsequently crushed. The phase purity of the samples was characterized using powder X-ray diffraction. Diffractograms were measured using a Panalytical Aeris diffractometer with Cu Kα radiation at 40 kV (λ =0.154 nm). It was demonstrated that YPO_4:15% Tb^{3+}, 2% Yb^{3+} consisted of a xenotime phase with some traces of unreacted precursors. YAG:0.1% Ce^{3+}, 5% Yb^{3+} was found to be a mixture of YAG and optically inactive alumina (see **??**).

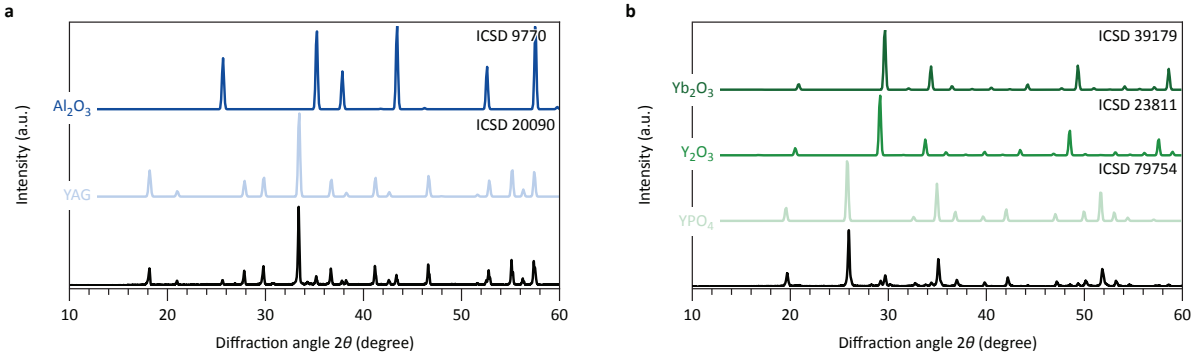

Figure S1. (a-b) Experimental powder X-ray diffraction pattern of **(a)** YAG:0.1% Ce^{3+}, 5% Yb^{3+} (black) with the corresponding reference patterns indicated by their ICSD collection codes. The sample consist predominantly of the desired YAG phase (light blue), with some traces of the Al_2O_3 precursor (dark blue). **(b)** Same as **a** but for YPO_4:15% Tb^{3+}, 2% Yb^{3+} (black). The sample shows mainly YPO_4 reflections (light green). Some additional signal can be observed from the unreacted precursors Y_2O_3 (green) and Yb_2O_3 (dark green)

S2 Single-photon time correlation measurements

Time-correlated single-photon counting measurements were performed using a home-built microscope setup. The YAG:0.1% Ce^{3+}, 5% Yb^{3+} and YPO_4:15% Tb^{3+}, 2% Yb^{3+} sample were excited using an OBIS 445LX CW and a OBIS 488LX CW laser, respectively. The excitation light was

focused on the sample using a Nikon CFI Plan Apochromat Lambda D 100× oil–immersion objective. The light emitted by the sample was collected by the same objective and imaged with a 19-mm lens (Thorlabs AC127-019-B-ML) onto two avalanche photodiodes (Thorlabs SPDMH2), arranged in a Hanbury-Brown–Twiss setup (Thorlabs BSW11R 50:50 beamsplitter plate). The signals from the single-photon-sensitive photodiodes are registered and time tagged by a quTools quTAG time-to-digital converter. The output of this device is a list with the timing of millions of photons detection events with 1 ps timing resolution. Correlations in this photon stream are analyzed and corrected for detector artifacts (deadtime, afterpulsing, afterglow) using the strategies detailed in the Supporting Information, Section S7. To isolate the NIR emission light, reflected excitation and visible emission light was blocked by placing a 650-nm dichroic (Thorlabs DMLP650R), a 500-nm longpass (Thorlabs FELH0500) and 950-nm longpass (Thorlabs FELH0950) filter in the detection path. To correct for defocusing during the measurement, the sample was scanned along the z-axis after every hour using a piezo stage (Mad City Labs Nano-LPS300) and moved to the position corresponding to the highest intensity.

S3 Spectroscopic measurements

Photoluminescence excitation and emission spectra were measured using an Edinburgh Instruments FLS920 fluorescence spectrometer equipped with TMS300 monochromators. The sample was excited using a 450-W xenon lamp. Spectra in the emission range 400–700 nm were recorded using a Hamamatsu R928 photomultiplier tube, whereas spectra in the emission range 850 to 1100 nm were recorded using a liquid-nitrogen cooled Hamamatsu H74422-40 photomultiplier tube. All emission and excitation spectra were corrected for the spectral response of the gratings and detector. Photoluminescence lifetime measurements were recorded on the same setup as used for time-correlated single-photon measurements. Yb^{3+} ions were resonantly excited with an OBIS 980LX laser operated in pulse mode. The laser was driven by a Aim-TTi TGA1244 waveform generator sending pulses with a 67 Hz repetition rate and a pulse width of 10 µs. Reflected excitation light was filtered out from the emission light by placing 1000-nm longpass filter in the detection arm (Thorlabs FELH1000).

S4 Setup collection efficiency

We estimate the collection efficiency for 980-nm light for our setup by coupling a 980–nm laser into the microscope and taking the ratio between laser intensity at the sample and the intensity recorded at the detectors. The average laser power at the sample position was measured to be $P_{\text{laser}} = 5.1$ µW, with a Thorlabs power meter (PM100D) and microscope slide photodiode power Sensors (S170C). From this we determine the maximum possible detector count rate (for a hypothetical collection efficiency of $\eta_{\text{col}} = 100$ %) at:

$$k_{\text{count}}^{\text{max}} = \frac{P_{\text{laser}}}{hc/\lambda} \tag{1}$$

h is Planck's constant, c the speed of light and λ the laser wavelength. The laser light was directed to the APDs by placing a silver mirror on the sample position. Additionally, two neutral-density filters (optical density $= 3.28$ at 980 nm) were placed in the collection arm, to prevent saturation of the APD pixels. Fig. S2 shows the intensity traces of the APDs. We find average count rates of $k_{\text{count}}^{1} = 1.73 \times 10^5$ s^{-1} and $k_{\text{count}}^{2} = 1.74 \times 10^5$ s^{-1}. Using the relation $\eta_{\text{col},i} = k_{\text{count}}^{i} 10^{\text{OD}} / k_{\text{count}}^{\text{max}}$, we estimate the efficiencies to be $\eta_{\text{col},1,2} = 2.5$ %.

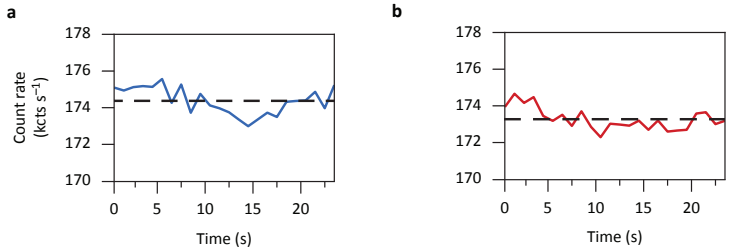

Figure S2. (a-b) Intensity trace of 980-nm laser light reflected to APD 1 and APD 2 from the sample location. The black dashed line shows the average count rate during of the measurement.

With the single–detector collection efficiencies we can calculate the pair collection efficiency of our setup. We discern two scenarios for pair detection. One where both photons are detected by the same APD, and one where the photons from a pair are detected on separate APDs. The probability for the first scenario is $2\eta_{\text{col}}^2$ where the pair collection efficiency per detector is η_{col}^2. Similarly, for the second scenario the overall probability is $2\eta_{\text{col}}^2$. The first photon has a probability of $2\eta_{\text{col}}$ to be detected by either APD 1 or 2 while the second photon can be detected only by the opposite detector, resulting in a collection efficiency of η_{col} for the second photon. The $g^{(2)}$ in our analysis is constructed by cross-correlating the signals detected by APDs 1 and 2. Consequently, we observe only photon pairs as described in scenario two, leading to an overall pair collection efficiency of $2\eta_{\text{col}}^2 = 0.13$ %.

Similarly, we can calculate the probability to detect exactly one photon from a QC photon pair. This is given by the product of the single-photon detection probability ($2\eta_{\text{col}}$) and the probability to miss the other photon ($1 - 2\eta_{\text{col}}$). Taking into account permutations, we find that the resulting probability for our setup is $4\eta_{\text{col}}(1 - 2\eta_{\text{col}}) = 9.5\%$.

S5 Intensity traces

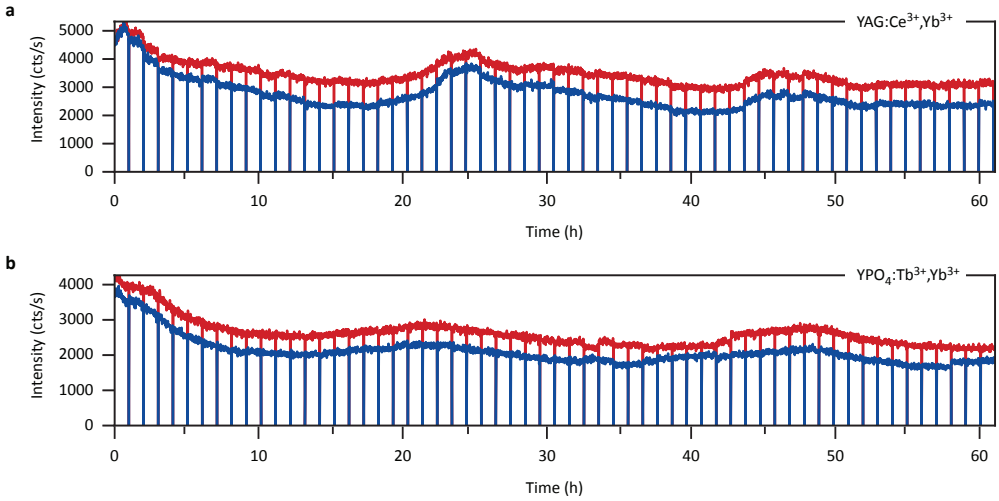

Figure S3. (a-b) Intensity traces of the signal on APD 1 (red) and APD 2 (blue) during a 60-h measurement for **(a)** YAG:Ce^{3+},Yb^{3+} and **(b)** YPO_4:Tb^{3+},Yb^{3+}. Drift along the optical axis causes the sample to defocus over time. To compensate for this the sample is refocused automatically every hour. The data collected during refocusing is omitted from the intensity traces and data analysis. Another source of count rate fluctuations is lateral drift of the sample. For both measurements the lateral drift was less than 2 µm over the course of the entire experiment, as determined by comparing a luminescence image of the sample before and after the measurement.

S6 Saturation

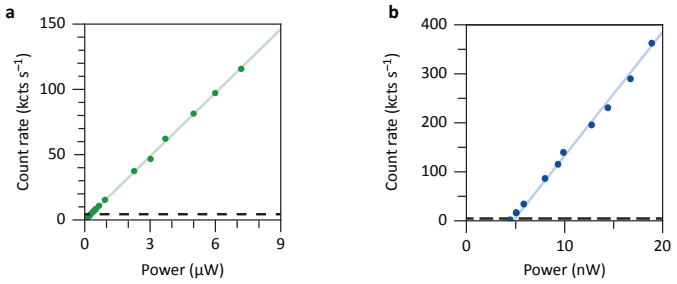

Figure S4. (a) Count rate of Yb^{3+} emission as a function of laser power for YPO_4:Tb^{3+},Yb^{3+}. The solid line shows a linear dependence up to count rates exceeding 10^5 cts s^{-1}. The dashed line represents the maximum count rate during the correlation measurements presented in the main text. We conclude that the sample is well below the saturation threshold. (**b**) Same as **a**, but for YAG:Ce^{3+},Yb^{3+}. We need significantly lower laser powers than in a because the absorption cross section of Ce^{3+} is larger than Tb^{3+}. In fact, the laser powers are so low that a background level on our power measurement creates an offset in the x axis of the plot. Nevertheless, the linear dependence of count rate on laser power up to 10^5 cts s^{-1} is clear, demonstrating that we operate below the saturation regime.

S7 Detector artifact correction

We estimate the probability p^i_{ap} of afterpulsing (Fig. S5b) on APD i from the non-Poissonian signal in the auto-correlation function:

$$p^i_{\text{ap}} = N^i_{\text{ap}}/2N^i. \tag{2}$$

Here, N^i_{ap} is the number of photon pairs due to afterpulsing in the auto-correlation function of APD i—i.e., the photon pairs in the shaded regions in Figs. S5f,g, which appear as a peak on top of the flat background—and N^i is the total number of photons detected on APD i. We find afterpulsing probabilities of $p^1_{\text{ap}} = 3.9\%$ and $p^2_{\text{ap}} = 3.3\%$. The afterpulsing probabilities are considerably higher than the probability that a detection event is followed by a correlated photon due to QC, which we estimate at $\eta^{\text{eff}}_{\text{col},i}/2 \approx 0.3\%$ (see Supplementary Section 5 below). To prevent that afterpulsing overwhelms real correlation signal in the experiment, we use two APDs in a Hanbury-Brown–Twiss setup and construct the $g^{(2)}$ from the cross-correlation of the photon streams of both APDs. The cross-correlation function still contains correlation artifacts due to afterglow (Fig. S5c), as light generated by APD 1 upon a detection event may travel through the optical setup and trigger a fake count on APD 2. We determine the probability p^{12}_{ag} that a detection event on APD 1 generates an afterglow event on APD 2 from the uncorrected cross-correlation function (Fig. S5e):

$$p^{12}_{\text{ag}} = N^{12}_{\text{ag}}/N^1 = 0.2\%, \tag{3}$$

where N^{12}_{ag} is the number of afterglow photon pairs in the cross-correlation function at delay times $0 < \Delta\tau < 43$ ns (red shaded area in Fig. S5g; above the flat background) and N^1 is the total number of photons detected on APD 1. Similarly, the probability p^{21}_{ag} that a detection event on APD 2 generates an afterglow event on APD 1 is

$$p^{21}_{\text{ag}} = N^{21}_{\text{ag}}/N^2 = 0.3\%. \tag{4}$$

Here, N^{21}_{ag} are the afterglow photon pairs at negative delay times 43 ns $< \Delta\tau < 0$ and N^2 are the photons detected on APD 2.

The afterglow events highlighted in Fig. S5g are easily removed from the analysis by removing any correlation counts with a delay time shorter than 43 ns, corresponding to the maximum recombination time of trapped carriers plus the travel time for photons through the optical setup. This does, however, not completely remove artifacts. A combination of afterglow and afterpulsing, as illustrated in Fig. S5h, can still produce fake correlations in the cross-correlation function. Specifically, a click on APD 1 (event 1) can cause an afterglow photon to be emitted, which travels through the setup and causes an afterglow click on APD 2 (event 2). This, in turn, can trigger an afterpulsing event on APD 2 (event 3). The sequence of events may also be reverse: an afterpulse on APD 1 (event 2) may generate an afterglow photon that is detected on APD 2 (event 3). The combined probability for these processes is $p^{12}_{\text{ag}}p^2_{\text{ap}} + p^1_{\text{ap}}p^{12}_{\text{ag}} = 0.018\%$. The probability that an APD click is followed by sequential afterglow and afterpulsing (Fig. S5g) is significantly lower than the probability of a second detection event due to QC (which is $\eta^{\text{eff}}_{\text{col},i}/2 \approx 0.3\%$, see above).

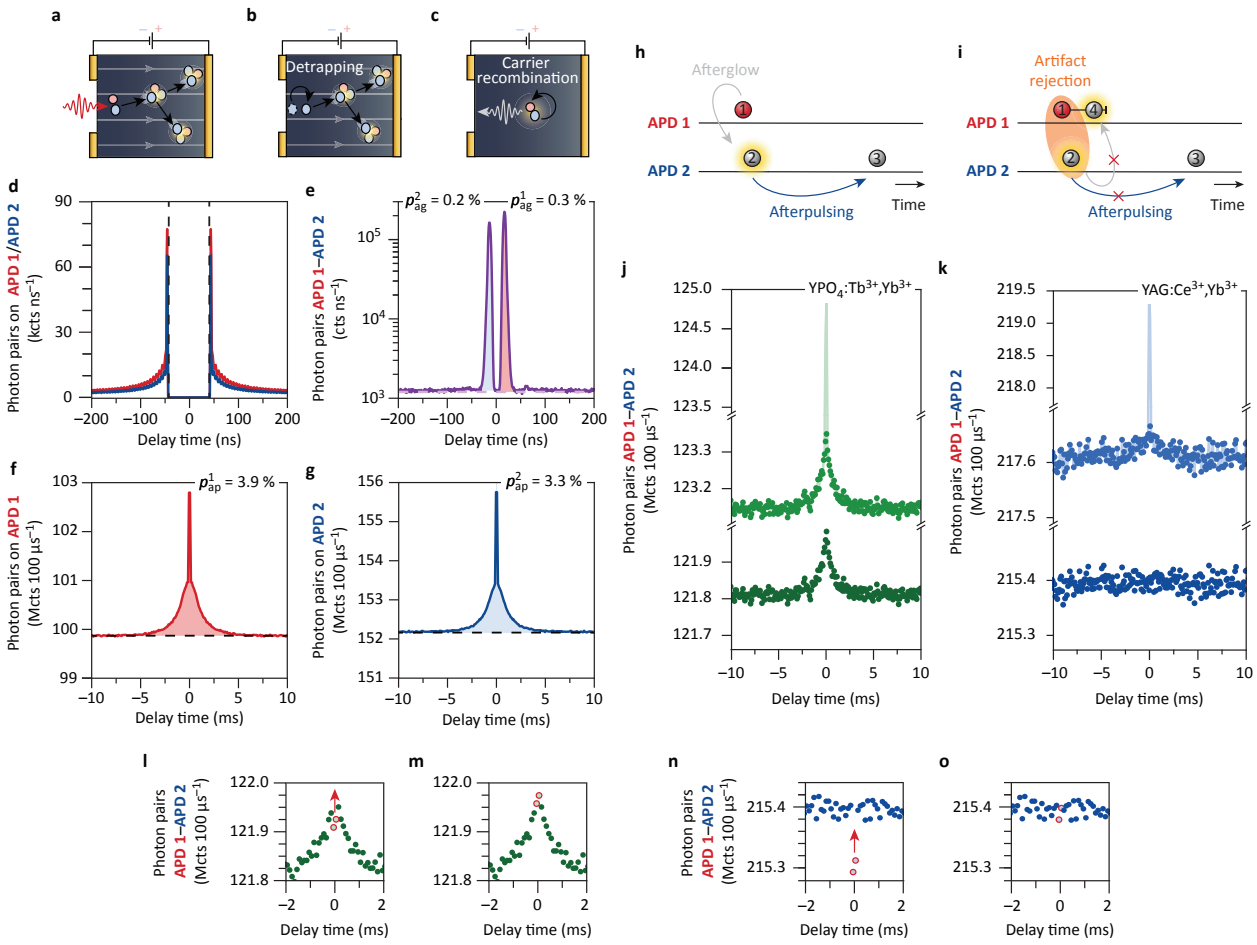

Figure S5. **(a-c)** Cartoons of an APD while it **(a)** detects a real photon, **(b)** detects an afterpulsing event and **(c)** emits an afterglow photon. **(d)** Auto-correlation functions of the photon stream on APD 1 (red) and the photon stream on APD 2 (blue), of the 60-h experiment on YPO_4:Tb^{3+},Yb^{3+}. No photon pairs are detected with delay times shorter than the detector dead time (black dashed lines). **(e)** Cross-correlation of APD 1 and APD 2. The shaded area above the Poissonian background (pink dashed line) stem from afterglow photons. Afterglow photons at negative delay times originate from APD 2 and at positive delay times from APD 1. **(f-g)** Auto-correlation function of photons detected on APD 1 (red) and APD 2 (blue) on a timescale of milliseconds. The non-Poissonian contribution (shaded area) above the background level (dashed line) stems from afterpulsing events. **(h)** Cartoon of coupling of the two APDs via afterpulsing following afterglow. 1 is a real photon detected by APD 1. It causes afterglow, which is detected as event 2 by APD 2, a few ns later. APD 2 shows afterpulsing that causes a new avalanche a few ms later. **(i)** In our analysis procedure we reject events 1 and 2 from the detection stream entirely. All pairs involving either 1 or 2, including the fake correlated signal pair 1–3, are thereby removed. **(j)** Uncorrected and corrected cross-correlation functions for YPO_4:Tb^{3+},Yb^{3+}. Solid line: the uncorrected data, showing a strong peak around $t = 0$ due to afterglow. Light-colored data points: after correction by rejecting photon pairs with delay times shorter than 43 ns. **(k)** Same as **j**, but for YAG:Ce^{3+},Yb^{3+}. The last correction step removes a small bunching feature in the uncorrected data (compare light-shaded and dark-shaded data points), which we ascribe to an artifact due to sequential afterglow and afterpulsing.(**l**) Correlation function for YPO_4:Tb^{3+},Yb^{3+} after artifact rejection by time gating. (**m**) Same as **l**, but now corrected for missed photon pairs due to time gating. (**n**,**o**) Same as **l**,**m**, but for YAG:Ce^{3+},Yb^{3+}.

Nevertheless, on a sample that does *not* exhibit QC, fake correlations due to sequential afterglow and afterpulsing are the only source of bunching. They prevent that the cross-correlation function becomes entirely flat, which may be misinterpreted as a signature of QC. To eliminate correlation artifacts due to sequential afterglow and afterpulsing, we remove any photons from the photon stream that are within a delay time of 43 ns from a photon on the opposite detector. These photons may originate from afterglow, and should be eliminated from the analysis procedure. This elimination procedure is stricter than removing the photon pair from the cross-correlation function. Rejecting both photons from the stream also removes any other pair that contains either photon. The fake correlation between event 1 and event 3 of sequential afterglow and afterpulsing is thus rejected (Fig. S5i), as desired. Figs. S5j,k show the uncorrected and corrected cross-correlation functions of YPO_4:Tb^{3+},Yb^{3+} and YAG:Ce^{3+},Yb^{3+}. In the uncorrected $g^{(2)}$ we observe a large spike centered around $t = 0$. This correlation stems from afterglow events. Gating the photon pairs with delay times up to the dead time of 43 ns removes this sharp peak. The YAG:Ce^{3+},Yb^{3+} still shows a weak bunching signal (Fig. S5k). We ascribe this to sequential afterglow and afterpulsing. Indeed, removing all photons that are within 43 ns of a photon on the opposite detector, removes this weak bunching feature. Although the bunching signal of YAG:Ce^{3+},Yb^{3+} before the last correction step is small, it is essential to remove this with proper data treatment to avoid a false positive conclusion.

Our artifact rejection procedure (Fig. S5i) prevents the detection of any photon pairs with delay times shorter than the dead time of $t_{\text{dead}} = 43$ ns. This removes artifacts but also removes any real photon pairs with such short delay times. As a result, the number of photon pairs in bins closest to $t = 0$ in the artifact-corrected correlation functions of YPO_4:Tb^{3+},Yb^{3+} (Fig. S5l) and YAG:Ce^{3+},Yb^{3+} (Fig. S5n) is suppressed by a small amount. We correct for this by multiplying the number of photon pairs in these two time bins by a factor $\delta t/(\delta t – t_{\text{dead}})$, where δt is the width of a time bin in the correlation function. This procedure assumes that the correlation function is approximately constant between $t = -\delta t$ and $t = +\delta t$, which is reasonable because the Yb^{3+} excited-state lifetime (0.6–0.9 ms) is much longer than the bin width (100 µs). The success of this final correction step is confirmed by the clear exponential bunching peak for YPO_4:Tb^{3+},Yb^{3+} (Fig. S5m) and the flat correlation function (apart from noise) for YAG:Ce^{3+},Yb^{3+} (Fig. S5o)

S8 Uniform excitation and detection

The quantum-cutting phosphors we use, contain lanthanide sensitizers and activators doped throughout the material.

The first simplified model for the expected bunching signal describes a situation where we excite a piece of material uniformly and emission generated at each position in the material has an equal probability to be detected. The count rate on detector i is

$$\bar{I}_i = k_{\text{exc}}\eta_{\text{em}}\eta_{\text{col},i} + D_i, \tag{5}$$

where $i = 1, 2$ labels the two detectors, $\eta_{\text{col},i}$ is the photon collection and detection efficiency on detector i, η_{em} is the emission efficiency of an activator ion, and D_i is the dark-count rate on detector i. The overall excitation rate of activator ions:

$$k_{\text{exc}} = k_{\text{abs}}N_{\text{sens}}\eta_{\text{ET}} \tag{6}$$

is dependent on the rate of absorption of excitation light per sensitizer ion k_{abs}, with the number of sensitizer ions illuminated N_{sens}, and with the efficiency of energy transfer from sensitizer to activator η_{ET}.

In principle, with carefully calibrated instrumentation and one could calculate η_{ET} directly from a measurement of I_i and $k_{\text{abs}}N_{\text{sens}}$. This could prove quantum cutting if $\eta_{\text{ET}} > 1$. Photon-bunching measurements prove or disprove quantum cutting without relying on error-prone calibrations of the various parameters in the above equations.

If the sample is a quantum-cutting phosphor, then we expect bunched photon emission: photons are emitted in pairs, as activator ions are excited two at a time. A photon-detection event on detector 1 at time $\tau = 0$ has a probability of

$$P_1 = \frac{1}{2}\frac{\bar{I}_1 - D_1}{\bar{I}_1} \tag{7}$$

to be the first photon of a photon pair. If it is, this signals that one of the many activators in the sample is in the excited state. Following the detection of 1, this one additional activator will decay with a rate constant of k_{dec} . As the total number of activators is much larger than unity, $N_{\text{act}} \gg 1$, the signal rate from all other activators remains as described by Eq. 5. The expected count rate on detector 2 is the sum of steady-state count rate (Eq. 5) plus the count rate due to the one additional excited activator:

$$I_2(\tau) = \bar{I}_2 + P_1\eta_{\text{col},2}\eta_{\text{em}}k_{\text{dec}}\mathrm{e}^{-k_{\text{dec}}\tau}. \tag{8}$$

This expression describes that following a detection event on detector 1, detector 2 registers an average number of excess photons equal to

$$n_{\text{extra}} = \int_0^\infty \left[I_2(\tau) - \bar{I}_2\right] \mathrm{d}\tau = P_1\eta_{\text{col},2}\eta_{\text{em}}. \tag{9}$$

The registration of the second photon of a pair occurs only if the photon on detection one was the first (probability P_1), if the second activator decays radiatively (probability η_{em}), and if the second photon is successfully collected and detected (probability $\eta_{\text{col},2}$).

We quantify the increased photon count rate on detector 2 following an event on detector 1 with the normalized photon correlation function

$$g^{(2)}(\tau) = \frac{\langle I_1(t) I_2(t+\tau)\rangle_t}{\langle I_1(t)\rangle_t \langle I_2(t+\tau)\rangle_t} = \frac{\bar{I}_1 I_2(\tau)}{\bar{I}_1 \bar{I}_2} = 1 + \frac{\eta_{\text{em}} k_{\text{dec}}}{2} \frac{\bar{I}_1 - D_1}{\bar{I}_1} \frac{\eta_{\text{col},2}}{\bar{I}_2} \mathrm{e}^{-k_{\text{dec}}\tau}, \tag{10}$$

where the averaging $\langle\cdot\rangle_t$ goes over the experiment time t. If the dark-count rates on the detectors are negligible compared to the photon counts, this expression simplifies to

$$g^{(2)}(\tau) \approx 1 + \frac{\eta_{\text{em}} k_{\text{dec}}}{2} \frac{\bar{I}_1}{\bar{I}_1} \frac{\eta_{\text{col},2}}{\bar{I}_2} \mathrm{e}^{-k_{\text{dec}}\tau} = 1 + \eta_{\text{em}} \eta_{\text{col},2} \frac{k_{\text{dec}}}{2\bar{I}_2} \mathrm{e}^{-k_{\text{dec}}\tau} \tag{11}$$

We can use this expression to predict the expected bunching amplitude, depending on the experimental count rate $\bar{I}_2$ and for different values of the product $\eta_{\text{em}}\eta_{\text{col},2}$. The uncorrelated background in the $g^{(2)}$ function contains $\bar{I}_1 \bar{I}_2 T \delta t$ photon pairs per time bin of width δt and for a total experiment duration of T. The Poissonian noise on these photon-pair counts is $\sigma = \sqrt{\bar{I}_1 \bar{I}_2 T \delta t}$, so the relative noise is

$$\sigma = \frac{1}{\sqrt{\bar{I}_1 \bar{I}_2 T \delta t}}. \tag{12}$$

Non-uniform excitation and detection

In our experiment, the illumination laser is focused and the detector collects signal from a finite volume of the sample. We account for this with a position-dependent excitation of activator ions and a position-dependent collection efficiency. Specifically, we define the position-dependent excitation-rate density

$$\kappa_{\text{exc}}(\mathbf{r}) = \frac{k_{\text{exc}}}{(2\pi\sigma_\rho \sigma_z)^{3/2}} \exp\left[-\frac{1}{2}\left(\frac{\rho}{\sigma_\rho}\right)^2 - \frac{1}{2}\left(\frac{z}{\sigma_z}\right)^2\right]. \tag{13}$$

as an elongated 3D Gaussian of a width σ_ρ in the plane normal to the optical axis and a width σ_z along the optical axis, expressed in cylindrical coordinates and centered at $(\rho_0, z_0) = (0, 0)$. The function $\kappa_{\text{exc}}(\rho, z)$ is such that the integral over all space equals the total excitation rate:

$$\int \kappa_{\text{exc}}(\mathbf{r})\, \mathrm{d}\mathbf{r} = k_{\text{exc}}. \tag{14}$$

We model the detection volume as a 3D Gaussian that is larger in linear dimensions by a factor f compared to the excitation volume and has a peak collection efficiency of $\eta_{\text{col},i}^{\text{max}}$:

$$\eta_{\text{col},i}(\mathbf{r}) = \eta_{\text{col},i}^{\text{max}} \exp\left[-\frac{1}{2}\left(\frac{\rho}{f\sigma_\rho}\right)^2 - \frac{1}{2}\left(\frac{z}{f\sigma_z}\right)^2\right]. \tag{15}$$

Eq. 10 is adapted to account for signals originating from different positions in the sample:

$$g^{(2)}(\tau) = \frac{\langle I_1(t) I_2(t+\tau)\rangle_{t,\mathbf{r}}}{\langle I_1(t)\rangle_{t,\mathbf{r}} \langle I_2(t+\tau)\rangle_{t,\mathbf{r}}}, \tag{16}$$

where $\langle\cdot\rangle_{\mathbf{r}}$ denotes integration of position. The separate integration over position of $I_1(t)$ and $I_2(t+\tau)$ in the denominator accounts for the possibility that two uncorrelated photons of a pair may be emitted from different positions of the sample. The single averaging of $I_1(t)I_2(t+\tau)$ in the numerator describes that the distance between the two activators excited by a quantum-cutting event is much smaller than the length scales σ_ρ, σ_z, so two correlated photons of a quantum-cut pair originate from the same position effectively. Again neglecting dark counts ($D_i \ll I_i$), we arrive at

$$g^{(2)}(\tau) \approx 1 + \frac{\eta_{\text{em}} k_{\text{dec}}}{2} \frac{\left\langle \bar{I}_1 \eta_{\text{col},2}\right\rangle_{\mathbf{r}}}{\left\langle \bar{I}_1\right\rangle_{\mathbf{r}} \left\langle \bar{I}_2\right\rangle_{\mathbf{r}}} \mathrm{e}^{-k_{\text{dec}}\tau}. \tag{17}$$

Here the position-integrated photon count rate on detector i (neglecting dark counts) is

$$\left\langle \bar{I}_i\right\rangle_{\mathbf{r}} = \eta_{\text{em}} \int \kappa_{\text{exc}}(\mathbf{r}) \eta_{\text{col},i}(\mathbf{r})\, \mathrm{d}\mathbf{r} = \eta_{\text{em}} k_{\text{exc}} \eta_{\text{col},i}^{\text{max}} \frac{f^3}{(1+f^2)^{3/2}}, \tag{18}$$

while the position-integrated photon-pair count rate (neglecting dark counts) is

$$\eta_{\text{em}} \left\langle \bar{I}_1 \eta_{\text{col},2}\right\rangle_{\mathbf{r}} = \eta_{\text{em}}^2 \int \kappa_{\text{exc}}(\mathbf{r}) \eta_{\text{col},1}(\mathbf{r}) \eta_{\text{col},2}(\mathbf{r})\, \mathrm{d}\mathbf{r} = \eta_{\text{em}}^2 k_{\text{exc}} \eta_{\text{col},1}^{\text{max}} \eta_{\text{col},2}^{\text{max}} \frac{f^3}{(2+f^2)^{3/2}}, \tag{19}$$

Now we define the effective collection efficiency $\eta_{\text{col},2}^{\text{eff}}$ of the second photon of a correlated photon pair by

$$g^{(2)}(\tau) = 1 + \frac{\eta_{\text{em}} k_{\text{dec}}}{2} \frac{\eta_{\text{col},2}^{\text{eff}} \left\langle \bar{I}_1\right\rangle_{\mathbf{r}}}{\left\langle \bar{I}_1\right\rangle_{\mathbf{r}} \left\langle \bar{I}_2\right\rangle_{\mathbf{r}}} \mathrm{e}^{-k_{\text{dec}}\tau}. \tag{20}$$

Equating Eq. 11 and 20, we arrive at an expression for $\eta_{\text{col},2}^{\text{eff}}$:

$$\eta_{\text{col},2}^{\text{eff}} = \frac{\left\langle \bar{I}_1 \eta_{\text{col},2}\right\rangle_{\mathbf{r}}}{\left\langle \bar{I}_1\right\rangle_{\mathbf{r}}} = \left(\frac{1+f^2}{2+f^2}\right)^{3/2} \eta_{\text{col},2}^{\text{max}} \tag{21}$$

We observe that the effective collection efficiency $\eta_{\text{col},2}^{\text{eff}}$ approaches the maximum collection efficiency $\eta_{\text{col},2}^{\text{max}}$ as the detection volume increases ($f \to \infty$). In the limit of a very small detection volume ($f \to 0$), $\eta_{\text{col},2}^{\text{eff}}$ decreases to $\eta_{\text{col},2}^{\text{max}}/\sqrt{8} = 0.35\eta_{\text{col},2}^{\text{max}}$. For the estimates in the main text of the expected normalized bunching amplitude, we assume $f \approx 1$, so $\eta_{\text{col},2}^{\text{eff}} \approx 0.54\eta_{\text{col},2}^{\text{max}}$. Experimentally, we found that the collection efficiency for 980-nm laser light specularly reflected off a mirror at the sample position is 2.5 % (Fig. S2) on both APDs. The reflected laser light is directional so it all enters the objective. In contrast, Yb^{3+} luminescence from our phosphor samples is approximately isotropic so only ~ 50 % goes in the direction of the objective. From this consideration, we estimate that the maximum collection efficiency is $\eta_{\text{col}}^{\text{max}} \approx 2.5/2\ \% = 1.2\ \%$. Hence, the effective collection efficiency, including regions of the sample outside the detection focus (Eq.

21), is $\eta_{\mathrm{col}}^{\mathrm{eff}} \approx 0.6$ % on both APDs.

A hypothetical scenario where QC energy transfer and conventional one-to-one energy transfer coexist, can be described by adding a factor $2\eta_D/(2\eta_D + \eta_S)$ to P_1 in eq 9. Here, η_{D} is the probability that the sensitizer ion decays via a QC energy-transfer pathway and η_{D} that it decays via a conventional one-to-one energy-transfer pathway. This factor thus describes that an Yb^{3+} photon is one of a QC pair. The additional factor in P_1 carries through the derivation and introduces the same factor to the theoretical bunching amplitude A_{rel}. Eq 2 of the main text becomes

$$A_{\mathrm{rel}} = \frac{2\eta_{\mathrm{D}}}{2\eta_{\mathrm{D}} + \eta_{\mathrm{S}}} \frac{\eta_{\mathrm{em}} k_{\mathrm{dec}} \eta_{\mathrm{col},i}^{\mathrm{eff}}}{2\langle I_i \rangle} \tag{22}$$

Fig. S6 shows a comparison of the experimental bunching data to the predictions of eq 24 for a scenario where QC and conventional one-to-one energy transfer coexist.

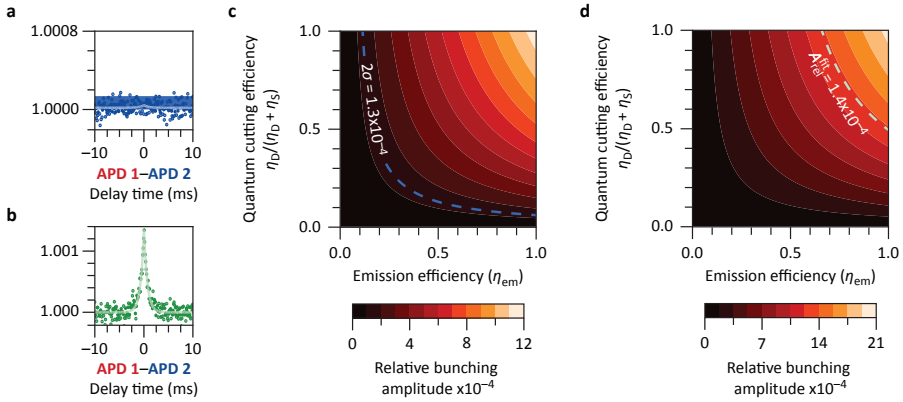

Figure S6. **(a)**) Experimental normalized second-order correlation function for YAG:Ce^{3+},Yb^{3+} and corresponding fit (line). The band shows the 2σ level of the background. (**b**) Same as for **a**, but for YPO_4: Tb^{3+},Yb^{3+}. (**c**) Relative bunching amplitude A_{rel} (color scale) as a function of the emission efficiency η_{em} and quantum-cutting efficiency relative to one-to-one energy transfer $\eta_D/(\eta_D + \eta_S)$, as predicted by eq 24. The isoline traces the 2σ level on the background. Any potential bunching is much weaker than this background level and not observable. (**d**) Same as for **c**, but for YPO_4: Tb^{3+},Yb^{3+}. The isoline shows the experimental bunching amplitude. In a hypothetical scenario where quantum-cutting and one-to-one energy transfer coexist, the experimental data is consistent with any combination of η_{em} and $\eta_D/(\eta_D + \eta_S)$ on the isoline. The Yb^{3+} lifetime (Fig. 1**e** in the main text) indicates an $\eta_{\mathrm{em}} = 66\%$, consistent with a quantum-cutting efficiency relative to total energy transfer of $\eta_D/(\eta_D + \eta_S) = 100\%$.